Cost Estimation and Agreement Worksheet

Click here to download Cost Estimation and Agreement Worksheet: cost_NYUAD.pdf

# Multi-scale interactions in an idealized Walker cell: analysis with isentropic streamfunctions

Joanna Slawinska *

*Center for Prototype Climate Modeling, New York University Abu Dhabi, Abu Dhabi, United Arab Emirates*

Olivier Pauluis and Andrew J. Majda

*Center for Atmosphere Ocean Science, Courant Institute of Mathematical Sciences, New York University, New York, NY*

Wojciech W. Grabowski

*National Center for Atmospheric Research, Boulder, CO*

**Corresponding author address:* PO Box 129188, Saadiyat Island, New York University Abu Dhabi, Abu Dhabi, United Arab Emirates

E-mail: joanna.slawinska@nyu.edu

ABSTRACT

We propose a new approach for analyzing multi-scale properties of the atmospheric flow that employs the recently introduced isentropic streamfunction and relies on its scale decomposition with Haar wavelets. We applied this method to a cloud resolving simulation of a planetary Walker Cell characterized by pronounced multi-scale flow. The resulting set of isentropic streamfunctions – obtained at the convective, mesoscale, synoptic, and planetary scales – captured many important features of the Walker Circulation. The convective scale was associated with the shallow, congestus, and deep clouds, which jointly dominate the upward mass flux in the lower troposphere. The synoptic and planetary scales played important roles in extending mass transport to the upper troposphere where the corresponding streamfunctions mainly captured the first baroclinic mode associated with large-scale overturning circulation. The intermediate scale features of the flow, such as anvil clouds associated with organized convective systems, were extracted with the mesoscale and synoptic scale isentropic streamfunctions. Multi-scale isentropic streamfunctions were also used to extract salient mechanisms that underlie the low-frequency variability of Walker Cell. In particular, the lag of a few days of the planetary behind the convective scale indicated the importance of the convective scale in moistening the atmosphere and strengthening the planetary-scale overturning circulation. Furthermore, the mesoscale and synoptic lags behind the planetary scale reflected the strong dependence of convective organization on shear.

## 1. Introduction

Convection is omnipresent throughout the Earth's atmosphere. Convective motions act to redistribute water and energy throughout the atmospheric column as warm, moist air rises within clouds, whereas drier and colder air subsides in the unsaturated environment. Convection itself occurs on relatively short and small scales, on the order of a few tens of kilometers and a few hours at most, but it interacts strongly with atmospheric flows on larger scales, such as synoptic waves and planetary circulations. The organization of convection over many scales is widely recognized (Mapes 1993). Mesoscale convective systems and synoptic scale convectively coupled equatorial waves are common examples of this type of organization. Other important phenomena include the Madden–Julien oscillation (Madden and Julian 1972), monsoonal flow, and the Hadley and Walker circulations.

These interactions across multiple scales remain challenging when modeling atmospheric flows. For example, relatively little is known about how convectively coupled waves are generated and maintained (Wheeler and Kiladis 1999, Yang et al. 2007, Khouider and Ham 2013, Roundy and Frank 2004, Stechmann et al. 2013, Dunkerton and Crum 1995). Large-scale conditions can strongly influence convective organization (Moncrieff 1981, 1992), which can have important implications for feedback at larger scales (Tung and Yanai 2002a, b; Wu and Yanai 1994, Houze et al. 2000). Numerical studies, such as Grabowski et al. (1996) and Wu et al. (1998), in which large-scale conditions were prescribed in given field experiments, showed that several convective systems (cloud clusters, squall lines, and scattered convection) emerged in a similar fashion to the actual observations. Mahoney and Lackmann (2011) showed that mesoscale convective systems are highly sensitive to environmental moisture. In their study, a drier atmosphere was associated with systems that are smaller, move faster, and that are more often associated with severe surface winds triggered by enhanced convective momentum transport. Del Genio el al. (2012) analyzed a cloud resolving model of convection with variable environmental humidity, which appears to play a major role in the time evolution of convective systems. Recently, Slawinska et al. (2014, SPMG hereafter) reported the strong dependence of convection, particularly its organization and feedback to other scales, on the idealized Walker Circulation, which exhibits low-frequency variability. The organization of convection at mesoscale and synoptic scales affects many other aspects of tropical weather and climate, e.g., approximately half of the precipitation in the tropics occurs within them (Del Genio and Kovari 2002, Schumacher and Houze 2003).

Thus, the appropriate parameterizations of convection and convective organization are urgently required in Global Climate Models (GCMs) (Moncrieff et al. 2012, del Genio el al. 2012). Numerous cumulus parameterizations have been developed and applied for decades. By contrast, according to our knowledge, only one cumulus parameterization with a representation of the mesoscale flow has been implemented in GCMs (Donner 1993, 2001). Despite significant improvements in capturing various aspects of global dynamics, there are still many flaws associated with these parameterizations. For example, most GCMs maximize precipitation over land at noon (Trenberth et al. 2003, Dai 2006) instead of late afternoon as indicated by observations. Remarkably, convective parameterizations have been argued to be the main culprit (Guichard et al. 2004, Rio et al. 2009; Del Genio and Wu 2010), where the entrainment coefficient is one of the main factors. Interestingly, Sanderson et al. (2010) showed that the entrainment coefficient caused the greatest climate sensitivity (based on an ensemble of one thousand simulations), mainly through water vapor feedback (Del Genio 2012). Another hypothesis, which is extremely challenging to verify, suggests that the absence of organization in convective parameterization does not allow convection to persist for a sufficiently long period.

It is hoped that high resolution simulations can help to address the convection problem. Nowadays, increase in computational resources allows convective motions to be resolved over a planetary-scale domain, however for a period of time insufficient to perform long-term climate simulations. Still, simulated period of time long is long enough to establish strong limitations associated with parameterization of convection in climate simulations.

To fully exploit new capabilities, we must first address the question of how to assess convective motions in high-resolution simulations. Moist convection is an extremely complex flow that involves motions at many scales, including subcloud layer turbulence, updrafts and downdrafts, anvil clouds, and convective overshoot. As with any turbulent flow, any 'mean' property depends on the averaging method employed. Recently, Pauluis and Mrowiec (2013, PM hereafter) proposed the use of isentropic analysis to systematically study convective motions in high-resolution climate models. Isentropic analysis dates back to the early development of synoptic meteorology (Bjerknes 1938) and its core idea assumes that entropy is approximately conserved in an atmospheric flow over a time scale of a few days. This means that it is possible to track the motions of air parcels over long distances on isentropic surfaces, even when the number of observations might be low. Averaging the flow on isentropic surfaces has also been used to capture mass transport by midlatitude eddies (e.g., Held and Schneider, 1999, and Pauluis et al. 2008, 2010). PM proposed the application of isentropic analysis to convective motions based on conditional averaging of the vertical mass transport in terms of the equivalent potential temperature of the air parcels. They used this procedure to study convective mass transport in high resolution simulations of radiative-convective equilibrium.

In PM, convective overturning is quantified in terms of an isentropic streamfunction, which is obtained as a domain integral, and thus it includes all scales of motion. The primary aim of the present study is to extend PMs framework to separate the contributions of individual atmospheric scales. This extended framework is then used to analyze the cloud resolving simulation of the planetary Walker Cell from SPMG. This idealized simulation exhibits a complex multi-scale flow, which resembles the tropical circulation in many respects. In particular, many organized convective systems are embedded within a large-scale flow with low-frequency variability, which shares many similarities with the intraseasonal oscillation that dominates tropical variability. We also illustrate how isentropic analysis can be used systematically to determine the contribution of various scales of motion to the global overturning circulation. In particular, we use it to quantify convective mass transport in high resolution global models.

The remainder of this paper is organized as follows. Section 2 presents a numerical simulation of the Walker Cell and its general features. Section 3 reviews the use of isentropic analysis to study moist convection, which was introduced by PM. PMs method is then extended to include a multi-scale decomposition of the flow, and used subsequently to analyze the overturning flow in the simulation. In Section 4, we discuss the low-frequency variability in the Walker circulation based on the isentropic analysis. Our conclusions are given in section 5.

## 2. Setup and main features of the simulated Walker Cell

SPMG use a two-dimensional version of the cloud resolving model EULAG (Grabowski 1998, Smolarkiewicz 2006, Prusa et al. 2008, Malinowski et al. 2011) to simulate an idealized Walker circulation. An atmospheric layer with a depth of 24 km is resolved over a horizontal domain of 40,000 km with horizontal and vertical resolution levels of 2 km and 500 m, respectively. The simulation is run over 320 days, where the last 270 days are analyzed based on statistics gathered at every time step (i.e., 15 s). The planetary-scale circulation is driven by the radiative tendency and surface fluxes. In particular, the prescribed radiative cooling tendency is the average NCAR CAM3 tendency in the radiative-convective equilibrium simulation performed with the

System for Atmospheric Modeling (Khairoutdinov and Randall 2003). Thus, radiative forcing (shown in Figure 1 in SPMG) results in 1.2 K day$^{-1}$ cooling of the troposphere and slight warming of the troposphere. An additional 20 days of relaxation of the potential temperature toward its environmental profile leads to additional cooling of the troposphere. Surface fluxes (see Equation 2 in SPMG) depend on the SST which varies between 303.15 and 299.15 K, where the warmest water is at the center of the domain, thereby mimicking the temperature contrast between the warm pool and colder equatorial upwelling region. A more detailed description of the setup is given in SPMG.

The simulated circulation shares many similarities with the Walker Cell in the tropics. The large-scale overturning flow comprises a deep-tropospheric ascent over the warm pool and subsidence over colder water, where the time-mean vertical velocities reach averages of up to 1.5 and 1 cm s$^{-1}$, respectively. The horizontal flow is characterized by low-level convergence in the ascent region, with an average velocity of 10 m s$^{-1}$. This is balanced by an outflow of about 20 m s$^{-1}$ in the upper troposphere. This planetary-scale overturning circulation can be captured by a Eulerian-mean streamfunction $\Psi_E$, which is defined as:

$$\Psi_E(x,z) = \frac{1}{L}\int_0^L \rho\overline{w(x,z')}dz', \tag{1}$$

where $L$ is the horizontal extent of the domain, $\rho(z)$ is the density of the air (which is only a function of height in the anelastic model that we employ), and $\overline{w}$ is the time-mean vertical velocity. To make a further comparison with mass transport at different scales, the Eulerian streamfunction is normalized by the domain size, and thus it is expressed in units of kg s$^{-1}$ m$^{-2}$. The Eulerian mean streamfunction is shown in Figure 1. The inflow below 6 km and outflow above 8 km peak at about 8000 km from the center of the domain. We also note a gradual lowering of the inflow as air moves toward the warm pool.

In addition to the Walker Cell, there is significant variability at the convective, meso-, and synoptic scales. For example, convection alternates between shallow, congestus, and deep convective regimes that occur over the convergence region, which is characterized by a high precipitable water content, although this is limited to the boundary layer over the colder ocean. Regions of intense convective activity are usually associated with strong meso- and synoptic scale systems, which frequently organize convection, as illustrated by the Hovmoller diagram of the cloud top temperature shown in Figure 2. A detailed discussion of these multi-scale interactions is given in SPMG, which demonstrates the strong coupling of two individual convective systems with planetary-scale properties. In particular, convective, mesoscale, and synoptic scale flows are highly intermittent in time and space, and they are mostly filtered by the spatial and temporal averaging used in the definition of the Eulerian streamfunction (see Equation 1 and Figure 1).

## 3. Isentropic analysis

### *a. Isentropic streamfunction*

A central motivation of the isentropic streamfunction defined by PM is capturing the contribution of the convective scales to vertical overturning in the atmosphere. This is achieved by conditionally averaging the vertical velocity in terms of the equivalent potential temperature $\theta_e$. The isentropic streamfunction is obtained by integrating the mass flux in the equivalent potential temperature over time period $T$ and area $L$:

$$\Psi_{\theta_e}(z, \theta_{e0}) = \frac{1}{T}\frac{1}{L}\int_0^T \int_0^L \rho(z) w(z,x,t) H(\theta_{e0} - \theta_e(x',z,t)) dx' dt, \tag{2}$$

where $w$ is the vertical velocity and $H$ is the Heaviside function. In this equation, $\theta_{e0}$ corresponds to the value of the equivalent potential temperature in the conditional average, while $\theta_e(x',z,t)$ is the equivalent potential temperature at a specific location and time. The conditional averaging in

(2) replaces the horizontal coordinates with the equivalent potential temperature. This approach discriminates warm and moist updrafts from colder, drier downdrafts of convective parcels. From a physical perspective, the streamfunction is equal to the net upward mass flux per unit area of all the air parcels with an equivalent potential temperature that is less than or equal to $\theta_{e0}$.

The isentropic streamfunction in Figure 3 exhibits many similarities to that presented in PM for radiative convective equilibrium. The streamfunction is negative, which indicates a descending motion for air with a low $\theta_e$ and an ascending motion for air with a higher $\theta_e$, where the flow transports energy upward. The isentropic streamfunction peaks near the surface, thereby indicating the preponderance of shallow convection. The mass transport decreases with height, which implies a significant detrainment. A very useful feature of the isentropic streamfunction is that its isolines correspond to the mean trajectories in the $\theta_e - z$ phase space, which means that it can be used to determine whether air parcels gain or lose energy (or more precisely, the equivalent potential temperature). In the lower troposphere, the equivalent potential temperature of rising air parcels decreases gradually with height due to entrainment and mixing of dry air in the updraft. Above the freezing level, rising air parcels exhibit a slight increase in $\theta_e$ due to the freezing of condensed water. Descending motions are typically linked to a reduction in $\theta_e$ due to radiative cooling. In a few areas, the equivalent potential temperature of the subsiding air increases, particularly for $2 \text{ km} < z < 3 \text{ km}$ and $315 \text{ K} < \theta_e < 335 \text{ K}$, and for $4 \text{ km} < z < 6 \text{ km}$ and $335 \text{ K} < \theta_e < 340 \text{ K}$, because these air parcels gain water vapor from diffusion. The reader should refer to PM for a more extensive discussion of isentropic analysis and the streamfunction.

In the present study, we are interested in comparing the isentropic streamfunction shown in Figure 3 and the Eulerian streamfunction in Figure 1. Therefore, in Figure 4, we also show the time-averaged equivalent potential temperature. The straight isolines stretching in $\theta_e - z$ phase space in Figure 3 between $\{z, \theta_e\} = \{9 \text{ km}, 345 - 355 \text{ K}\}$ and $\{z, \theta_e\} = \{2 \text{ km}, 320 - 335 \text{ K}\}$ correspond to the subsidence of dry air from the upper troposphere to the top of the boundary layer. A closer inspection of Figure 4 shows that the very low values of $\theta_e < 335$ K are associated with isentropic downward motion, which is a characteristic of air subsiding over the cold ocean. The ascending branch of the isentropic streamfunction occurs for large values of $\theta_e$, with $\theta_e > 355$ K. These values of the equivalent potential temperature are significantly larger than the time-averaged values $\theta_e$. Figure 4 shows that there is a mid-tropospheric minimum of about $345K$, which is much less than the value for the ascending air shown in Figure 3. In fact, Figure 3 captures that the air parcels with $\theta_e \approx 345$ K and $z = 4$ km move downward to a height of 3–5 km on average. This indicates that even in regions of mean ascent, the bulk of the air parcels, i.e., those where $\theta_e$ is close to its mean value, are moving down rather than up. Instead, the ascent occurs within narrow convective cores, the thermodynamic properties of which are not captured by the eulerian mean circulation

A major difference between the isentropic streamfunction and its Eulerian counterpart is the magnitude of mass transport. Indeed, the difference between the maximum and minimum value of the Eulerian streamfunction is about $1.4 \times 10^{-3}$ kg m$^{-2}$ s$^{-1}$. By contrast, the isentropic streamfunction indicates a mass transport of $7.5 \times 10^{-3}$ kg m$^{-2}$ s$^{-1}$. In addition, the peak of the mass transport for the Eulerian circulation is in the upper troposphere, whereas the isentropic streamfunction has its maximum near the surface. These differences occur mainly because the Eulerian streamfunction primarily captures the planetary scale flow, whereas the isentropic streamfunction aggregates the contributions at multiple scales.

### *b. Multi-scale decomposition of the isentropic circulation*

In this study, we analyze the contribution of various scales to the isentropic streamfunction as follows. First, the vertical velocity is decomposed into components associated with the spatial scales of interest. Second, isentropic averaging is performed and the corresponding isentropic streamfunction is constructed by integrating over the appropriate spatial and temporal boundaries for the given scale. We focus on four significant scales: convective, mesoscale, synoptic, and planetary, constrained as follows:

- 10,000 km < planetary scale
- 1,250 km < synoptic scale < 10,000 km
- 156 km < mesoscale < 1,250 km
- 2 km < convective scale < 156 km.

The choice of these scales is somewhat arbitrary, but they were motivated by the previous analysis in SPMG. The vertical velocity is decomposed into the contributions of these scales as:

$$w = w_{planetary} + w_{synoptic} + w_{mesoscale} + w_{convective}. \tag{3}$$

In principle, this decomposition corresponds to band filtering with Haar wavelets, which is applied as follows:

$$w_{planetary} = a_{0,0} + \sum_{i=i_1}^{i=i_2} \sum_{j=0}^{j=2^i-1} a_{i,j}\varphi_{i,j} \tag{4}$$

$$w_{synoptic} = \sum_{i=i_2}^{i=i_3} \sum_{j=0}^{j=2^i-1} a_{i,j}\varphi_{i,j} \tag{5}$$

$$w_{mesoscale} = \sum_{i=i_3}^{i=i_4} \sum_{j=0}^{j=2^i-1} a_{i,j}\varphi_{i,j}, \tag{6}$$

where $a_{0,0} = 0$ is the horizontal mean vertical velocity. The Haar functions $\varphi_{i,j}$ are defined as follows:

$$\varphi_{i,j}(x) = \varphi(2^i x - j) \tag{7}$$

$$\varphi(x) = 1 \text{ for } 0 < x < 20000$$

$$\varphi(x) = -1 \text{ for } 20000 < x < 40000.$$

The Haar wavelets act as a local filter, where its shape is described by the mother wavelet, its wavenumber band is determined by the parameter $i$, and the location where the given filter is applied is given by the parameter $j$. The convective velocity, $w_{convective}$, is defined as the difference between the instantaneous value of the vertical velocity and sum of the drafts associated with other scales.

Using the vertical velocities decomposed as described above, the streamfunction for a given scale is determined by Equation 2, where the vertical velocity is limited to the contribution of the corresponding scale. Thus, the isentropic streamfunction is decomposed into:

$$\Psi = \Psi_{planetary} + \Psi_{synoptic} + \Psi_{mesoscale} + \Psi_{convective}, \tag{8}$$

where every streamfunction is closed when the vertical velocity decomposition is applied as described above. Figure 5 shows the multi-scale isentropic streamfunctions collected every time step over 152 km, which were subsequently averaged over 273 days and 40,000 km.

The streamfunction associated with the convective scale, as shown in Figure 5a, captures the mass transport associated with shallow and deep convection. In particular, deep convective drafts leave clear imprints in the convective streamfunction in the form of isolines that connect the surface and the upper troposphere. If the equivalent potential temperature is 365 K or more, the isolines are almost vertical, particularly above the boundary layer, thereby reflecting the fact that the deep convective updrafts in a saturated environment (e.g., in a cloud core) can transport mass upward without significant dilution. For regions with an equivalent potential temperature around 360 K at the top of the boundary layer, the isolines starts to shift slightly in height toward the lower equivalent potential temperature and they reach lower altitudes. This is an indication of the entrainment of dry air into the clouds (see PM for more details) and detrainment. By contrast, the downdrafts associated with deep convection are also captured by the isolines stretching throughout the whole troposphere, but the average equivalent potential temperature is lower than 355 K. This decrease in the equivalent potential temperature is caused mainly by evaporative cooling due to rain falling from clouds or cloudy air detrained into environmental air at the edges of the clouds.

Shallow convection is quite prominent in Figure 5a. Significant mass transport below 2 km can be observed over a wide range of equivalent potential temperatures, thereby reflecting the fact that shallow convection occurs over both warm pool and cold ocean. The maximum convective streamfunction at an altitude of 1 km indicates that shallow convection is much more active than deep convection in moving the air around the atmosphere. The streamfunction is positive for 2 km $< z <$ 3 km and 315 K $< \theta_e <$ 335 K. This is a signature of the entrainment of warm free tropospheric air at the top of the planetary boundary layer in the subsidence region. As noted earlier, the mass transport associated with the convective scale is omitted completely from the Eulerian streamfunction.

Figure 5b shows the contribution of the mesoscale to mass transport, which corresponds primarily to organized convection, such as squall lines. Although the global mean in Figure 5 does not allow us to distinguish the mass transport associated with individual systems, their collective impact is reflected in the mesoscale streamfunction. There is a pronounced peak in the upper troposphere between 4 and 9 km, which reflects the distinctive overturning circulation that is often found in moist and warm regions that stretch for hundreds of kilometers at the rear of the organized systems referred to as anvil clouds. In these regions, the mesoscale updrafts are associated with stratiform clouds that often precipitate. Latent heat release within anvil clouds and evaporative cooling in the sub-cloud layer are often represented by the second baroclinic mode. This is indicated clearly by the numerous quasi-vertical isolines that join the middle and upper troposphere regions to the peak of the equivalent potential temperature at 350 K. In the lower troposphere, descent is associated with numerous isolines that connect the middle troposphere with the top of the boundary layer, which have roughly the same equivalent potential temperature within the range of 330–345 K. Interestingly, the secondary peak of the mesoscale streamfunction occurs at $\{\theta_e, z\} = \{350\ \mathrm{K}, 1\ \mathrm{km}\}$, which indicates that shallow convection within boundary layer causes some organization at the mesoscale.

The synoptic scales capture the mass transport associated with organized convection as well as planetary-scale overturning circulation. In particular, the straight isolines stretching between $\{\theta_e, z\} = \{350-355\ \mathrm{K}, 9\ \mathrm{km}\}$ and $\{\theta_e, z\} = \{330-340\ \mathrm{K}, 5\ \mathrm{km}\}$ may be related to the slow subsidence of dry air over cold ocean, which results in a $\theta_e$ decrease of 20 K due to radiative cooling. Subsequent moistening due to entrainment and mixing in the lower troposphere results in an $\theta_e$ increase of 20 K. The synoptic-scale isentropic streamfunction also captures the circulation associated with organized convective systems, i.e., convectively coupled equatorial waves. These systems often comprise the envelope of numerous mesoscale systems. Subsequently, the features of stratiform anvil clouds contribute to the maximum isentropic streamfunction at $\{\theta_e, z\} = \{345-350\ \mathrm{K}, 5-7\ \mathrm{km}\}$.

The planetary scale streamfunction mostly reflects a deep large-scale overturning circulation. In particular, deep tropospheric subsidence is captured by the straight isolines that connect the upper troposphere with the top of the boundary layer at an altitude of 2 km. Dry air with an initial equivalent potential temperature of 345–350 K slowly cools radiatively by more than 30 degrees by the time it reaches the lower troposphere. The circulation of mass is particularly strengthened between 6 and 9 km, which agrees with the circulation captured by the traditional approach (see Figure 1 and its discussion). Traditionally, large-scale subsidence is thought to be balanced by large-scale ascent over high $\theta_e$, e.g., as depicted by the Eulerian streamfunction (see the discussion above). However, a detailed comparison of the isentropic streamfunctions shows that the upward transport of high $\theta_e$ air is dominated by the convective scale. Thus, large-scale ascent is recognized as an artifact of the specific averaging method employed, which is an otherwise overlooked feature of the multi-scale flow of interest.

To compare the contributions of the individual scales more directly, we can define an isentropic mass transport as

$$M(z) = \max_{\theta_e}(\Psi(z,\theta_e)) - \min_{\theta_e}(\Psi(z,\theta_e)). \tag{9}$$

Figure 6 shows the mean mass fluxes calculated from the multi-scale isentropic streamfunctions shown in Figure 5 and discussed above. Although the decomposition of isentropic streamfunctions requires that the overall streamfunction is the sum of the contributions of all scales, the same does not apply to the mean mass fluxes:

$$M(z,\Psi) \le M(z,\Psi_{planetary}) + M(z,\Psi_{synoptic}) + M(z,\Psi_{mesoscale}) + M(z,\Psi_{convective}). \tag{10}$$

From a mathematical point of view, this is simply a consequence of the nonlinearity of the max/min function. From a physical point of view, this reflects the fact that the ascending and descending motions at different scales may occur at various values of $\theta_e$. For example, as discussed earlier, large-scale ascent occurs for $\theta_e \approx 345K$, but ascent at the convective scale occurs at much larger $\theta_e \approx 355K$. In these cases, the interactions at different scales result in a shift of $\theta_e$ for the rising air parcels toward higher values, rather than an increase in the mass transport.

Figure 6 shows unambiguously that the convective scale dominates the upward mass transport throughout the whole troposphere. This effect is especially pronounced in the lower troposphere because shallow and deep convection act intensively there, whereas the contributions from the other scales are negligible. In the upper troposphere, on the other hand, the contributions from the other scales are significant compared with the convective scale. In particular, the transport associated with synoptic and planetary scale is of a similar magnitude, where the maximum in the upper troposphere and the transporting mass flux are comparable to those at the convective scale. By contrast, the mesoscale accounts for only a small fraction of total mass transport. Thus, the convective scale accounts for most of the mass transport throughout the lower and middle troposphere, whereas the synoptic and planetary scales have significant impacts in extending this mass transport to the upper troposphere.

To compare the results obtained using different approaches, the mean mass flux obtained from the Eulerian streamfunction is also shown in Figure 6. It is larger than the mass transport estimated by the planetary scale isentropic streamfunction which indicates that the Walker Circulation includes contributions from both the planetary and synoptic scales.

### *c. Spatial variability*

So far, we described multi-scale properties of the circulation from a global point of view, as mass flux profiles have been obtained by averaging over the whole domain and simulated period. However, many of these characteristics can be retrieved and studied for as high spatial resolution as 152 km, 1250 km, and 10,000 km for convective, meso-, and synoptic scales, respectively. The isentropic mass transport from each scale can then be computed based on Equation 9, as shown in Figure 7.

The convective scale captures the tropospheric transport associated with both shallow and deep convection. The deep tropospheric transport of mass associated with deep convection occurs over 10,000 km of warm pool. Interestingly, although the horizontal distribution over this region is approximately uniform, regions located approximately 5000 km distant from the warmest SST are slightly more efficient in convective transport. This agrees with the finding reported in SPMG that the most intense convection occurs over regions with the strongest surface winds at the sides of the warm pool. The convective mass transport also shows the gradual strengthening and deepening of shallow convection when moving from the subsidence region to the warm pool.

The distribution of the mesoscale mass flux resembles that associated with the convective scale, although it is much weaker. As noted earlier, there is a significant contribution of the meso-scale mass transport in the boundary layer in the subsidence regions. This indicates that there is some organization of the shallow convection in these regions. The mesoscale mass transport exhibits a well-defined maximum at the edges of the warm pool, where the wind shear is the strongest. This local maximum is strongly pronounced in the upper troposphere. Moreover, in these regions, the mesoscale mass flux is of a similar magnitude to the corresponding one associated with the convective or synoptic scales. Although the mesoscale does not contribute greatly to the domain averaged mass transport, as shown in Figure 6, it can be locally significant.

The synoptic scale fluxes are significant over warm pool and very weak over subsidence regions, which agree with the fact that they are associated mainly with the synoptic scale in organized convective systems that propagate through the convergence region confined to the warm pool.

## 4. Low-frequency variability

As reported in SPMG, the Walker circulation in our simulation exhibits low frequency variability on an intraseasonal time scale. In SPMGS, this low-frequency variability is captured by the first EOF of the surface wind anomaly, which accounts for 36.3 % of the variance. Its spatial pattern and principal component (see Figure 7 in SPMG) correspond to the strengthening and weakening of the flow with a time period of approximately 20 days. Subsequently, we apply principal component to the first EOF and calculate lag-regression to the other variables, thereby reconstructing their temporal evolution. Following SPMG, we perform a lag regression of the isentropic streamfunction on the EOF index. The evolution of the low-frequency variability is then decomposed into four phases: a suppressed phase for lag $\tau \leq -8$ days and $\tau \geq 7$ days, an amplifying phase for $\tau \in \{-8;-3\}$ days, an active phase for $\tau \in \{-3;2\}$ days, and a decaying phase for $\tau \in \{2;7\}$ days. Their discussion in SPMG indicates that they are the dominant mechanisms that drive the cycle, which highlights the importance of their multi-scale nature. In the present study, we analyze the multi-scale properties of this low-frequency variability based on reconstructed fields using the multi-scale analyses introduced in the previous section.

Figure 8 shows the lag-regressed profiles of the globally-averaged mass fluxes associated with the convective, mesoscale, synoptic and planetary scales. The planetary scale circulation peaks at day zero consistently with the index of low-frequency variability, which is defined as the first EOF of the zonal wind. By contrast, the convective mass transport peaks before the maximum intensity between lag $-3$ and $-1$ day. This confirms that the convective precondition and moistening play important roles in strengthening the circulation. Conversely, the synoptic and meso-scale transport peaks occur later, with a lag of about 1 or 2 days. This suggests that these scales are intensifying, partly because of the more intense wind shear.

Figure 9 shows the streamfunctions at various scales, which were evaluated with a lag of $-1$ days, i.e., close to the peak intensity for both the convective and planetary scale. The convective mass flux is strengthened throughout the whole troposphere by as much as 25 percent above the average, thereby indicating significant invigoration from the shallow to congestus to deep convection, particularly in the regions associated with high $\theta_e$. This convective preconditioning of the large-scale environment leads to prominent strengthening of the planetary scale circulation by up to 45 percent at $\tau = -1$ day and it peaks one day later. There are also slight (10–20 percent) negative anomalies at high $\theta_e$ throughout the whole troposphere for the mesoscale and synoptic contributions, which may be associated with emergence of organized convective systems over the convergence region.

Figure 10 shows the anomalies associated with day $\tau = 4$, which correspond to the decaying phase of the large-scale circulation. Clearly, there is a shift in the circulation toward larger $\theta_e$ for all of the scales, which can be identified based on the dipole structure of the streamfunction anomaly. This reflects the fact that the whole atmosphere is anomalously warm after a period of prolonged heating due to enhanced latent heat release and heavy rain. The isentropic streamfunctions associated with the convective and planetary scale have a similar intensity to their time averages, but they are clearly shifted toward high values of $\theta_e$. The mesoscale and synoptic scales exhibit strengthening of their circulation with peaks at about day $\tau = 3$. This may be related to circulation within the organized convective systems that emerge during the active phase, which are reinforced by the large-scale wind shear.

Figure 11 shows the isentropic streamfunctions during the suppressed phase of the low-frequency variability at lag $\tau = 9$ day. The planetary circulation is at its weakest, where the corresponding transport declines to 45 percent below its time-averaged value. The weaker circulation is associated with weakening of the convective activity by about 20 percent, which indicates an abundance of convective activity even during the suppressed phase. Moreover, the weakened large-scale circulation disfavors convection organized over the mesoscale and synoptic scales, thereby resulting in positive and negligible anomalies in the corresponding streamfunctions. At the same time, there is a slight enhancement in the mesoscale and convective streamfunctions at low altitude and $\theta_e$. This strengthening of the boundary layer circulation may be associated with the invigoration of shallow convection due to weakening of the large-scale subsidence over the cold ocean.

Figure 12 corresponds to day $\tau = -6$ of the low-frequency oscillation in the strengthening phase. At this time, the upper troposphere is dry and cold after many days of suppressed convection, which is reflected by the positive anomalies over high $\theta_e$ in all the isentropic streamfunctions and by the subsequent overall shifts in the multi-scale streamfunctions toward lower $\theta_e$. At the same time, a negative anomaly in the convective streamfunction with lower $\theta_e$ occurs over the whole depth of the troposphere. The enhancement of the upward mass flux (see Figure 8) is associated with the ongoing intensification of deep convection, which is triggered by the large-scale zonal advection of anomalously moist air from the lower troposphere in subsidence regions. This moist air originates from the ongoing intensification of shallow convection, as shown by the increased mesoscale mass flux in the lower troposphere. The planetary scale circulation also starts to strengthen, especially in the upper troposphere. The synoptic and mesoscale streamfunctions are anomalously negative, where the mass fluxes that correspond to these scales are at their lowest, particularly in the upper troposphere. This corresponds to the scarcity of convective organization, which contrasts with the periods characterized by more favorable (e.g., strong shear) large-scale conditions.

## 5. Conclusions

In this study, we proposed a new method for analyzing the contributions of individual scales to atmospheric overturning. Thus, we performed a scale separation of the isentropic streamfunction introduced by PM. The isentropic streamfunction is defined as the net upward mass flux of all the air parcels at a given height with an equivalent potential less than a given threshold. PM used this technique to study convective motions in an atmosphere in radiative convective equilibrium, and showed that isentropic analysis can be used to determine many aspects of the circulation, such as mass transport, entrainment, and diabatic tendencies.

One of the limitations of the original formulation proposed by PM is that the streamfunction is defined as a global integral, and thus it includes the contributions of all scales. To address this issue, we used a set of Haar wavelets to perform a scale decomposition of the vertical velocity where we determined the isentropic streamfuction associated with each individual scale. This approach was applied to a high-resolution simulation of an idealized planetary-scale Walker Cell with the cloud-resolving model EULAG. This simulation exhibits a planetary scale overturning circulation, which is strongly coupled to convection. There is also significant organization of convection at the meso- and synoptic scales, and the overall circulation exhibits a low frequency variability with a period of about 20 days. These simulations were documented previously in SPMG and they provide a good test case for the scale interactions in the tropical atmosphere.

Our analysis emphasizes the difference between the Eulerian circulation obtained from the time-averaged velocity field in Eulerian $(x-z)$ coordinates and the isentropic streamfunction. In particular, the mass transport associated with the Eulerian circulation is one order of magnitude smaller than that obtained from the isentropic streamfunction. In addition, the isentropic analysis showed that the equivalent potential temperature of the ascending air is much larger than the time-averaged value of the equivalent potential temperature anywhere within the troposphere. We argue that these differences can be explained by the fact that the Eulerian averaging convective motions are filtered by Eulerian averaging whereas they are captured by the conditional averaging isentropic analysis.

This interpretation was also confirmed by the scale decomposition of the isentropic streamfunctions, where most of the isentropic streamfunctions could be attributed directly to the convective scales (less than 156 km). The convective scale was associated with shallow, congestus, and deep mass transport of high $\theta_e$, which jointly dominates the global mass flux upward throughout the lower troposphere. The mass transport at the convective scale peaked in the boundary layer and decreased gradually with height. The isentropic mass transport associated with meso-scale motions (between 156km and 1250km) was much weaker than any of the other scales, but it exhibited a peak in the upper troposphere, which is associated with rising motions in anvil clouds. The mass transports at the synoptic (between 1250 and 10,000 km) and planetary scales (larger than 10,000 km) were of comparable magnitude with a maximum in the upper troposphere, and they were also of comparable magnitude to transport by the convective scale. The overall picture that emerges from our analysis is that the convective scale dominates the overturning circulation, whereas the planetary and synoptic scales play significant roles in deepening the depth of the overturning flow.

Our approach also allowed us to define a local isentropic streamfunction and to quantify the mass transport by convective motions in high resolution simulations. In our idealized Walker simulation, we observed a gradual deepening of shallow convection to the edge of the warm pool, followed by a sharp transition toward deep and intense convection. Similarly, our analysis of the low frequency variability showed that convective activity preceded the strongest overturning circulation by a couple of days, which was associated with a gradual preconditioning and moistening of the free troposphere before the strongest large scale winds could be established. By contrast, the mass transport at the meso- and synoptic scales peaked a few days after the maximum of the planetary scale circulation, which indicates that convective organization on these scales is primarily driven by vertical wind shear. While these results are specific to our simulation, they demonstrate the potential use of isentropic analysis to study convective motions and their interactions with the other atmospheric scales in high resolution simulations.

The isentropic framework developed by PM analyzes atmospheric overturning by conditionally averaging vertical motions in terms of the equivalent potential temperature. This approach is particularly well suited to studying the interactions between convection and larger scales. In addition to PM, several studies (Zika et al. 2012, Kjelsson et al. 2014, Laliberté et al. 2015) have used similar conditional averaging based on different thermodynamic variables (temperature, entropy, and salinity) to study the atmospheric circulation, thereby obtaining novel insights into the atmospheric flow. In contrast to more traditional studies of the meridional circulation in various coordinates (Townsend and Johnson, 1985, McIntosh and McDougall 1996, Held and Schneider, 1998, Pauluis et al., 2008, 2010), which rely solely on the meridional wind, these studies require detailed information about the vertical velocity field. However, these studies were typically based on large-scale atmospheric or oceanic datasets that do not resolve the convective scale. Therefore, these studies are limited by the fact that these datasets can only provide information about overturning at larger scales whereas they ignore the contribution of the convective scale. As demonstrated in the present study, the mass transport by convection is typically much larger than the transport due to the flow at larger scales and it accounts for the bulk of atmospheric overturning.

## 6. Acknowledgments

J. Slawinska acknowledges funding from the Center for Prototype Climate Modeling at New York University Abu Dhabi. This research was carried out on the high performance computing resources (http://nyuad.nyu.edu/en/research/infrastructure-and-support/nyuad-hpc.html) at New York University Abu Dhabi.

## 7. References

Bjerkness, J., 1938: Saturated-adiabatic ascent of air through dry-adiabatically descending environment. Quart. J. Roy. Meteor. Soc., 64, 325-330.

Dai, A., 2006: Precipitation characteristics in eighteen coupled climate models. J. Climate, 19, 4605-4630.

Del Genio, A.D., and W. Kovari, 2002: Climatic properties of tropical precipitating convection under varying environmental conditions. J. Climate, 15, 2597-2615.

Del Genio A.D., and J. Wu, 2010: The role of entrainment in the diurnal cycle of continental convection. J. Climate, 23, 2722-2738.

Del Genio, A. D., J. Wu and Y. Chen, 2012: Characteristics of Mesoscale Organization in WRF Simulations of Convection during TWP-ICE. J. Climate, 25, 5666-5688.

Del Genio, A.D., 2012: Representing the sensitivity of convective cloud systems to tropospheric humidity in general circulation models. Surv. Geophys., 33, 637-656. doi:10.1007/s10712-011-9148-9.

Donner, L. J., 1993: A Cumulus Parameterization Including Mass Fluxes, Vertical Momentum Dynamics, and Mesoscale Effects. J. Atmos. Sci., 50, 889-906.

Dunkerton, T.J., and Crum, F.X, 1995: Eastward propagating 2- to 15-day equatorial convection and its relation to the tropical intraseasonal oscillation. J. Geophys. Res., 100(D12), 25781-25790.

Grabowski W.W., Wu X., and M. W. Moncrieff, 1996: Cloud-Resolving Modeling of Tropical Cloud Systems during Phase III of GATE. Part I: Two-Dimensional Experiments. J. Atmos. Sci., 53, 3684-3709.

Grabowski, W. W., 1998: Toward cloud resolving modeling of large-scale tropical circulations: A simple cloud microphysics parameterization. J. Atmos. Sci., 55, 3283-3298.

Guichard, F., Petch, J. C., Redelsperger, J.-L., Bechtold, P., Chaboureau, J.-P., Cheinet, S., Grabowski, W., Grenier, H., Jones, C. G., Khler, M., Piriou, J.-M., Tailleux, R. and Tomasini, M., 2004: Modelling the diurnal cycle of deep precipitating convection over land with cloud-resolving models and single-column models. Q. J. R. Meteorol. Soc., 130, 3139-3172. doi: 10.1256/qj.03.145

Held, I. M and T. Schneider, 1999: The Surface Branch of the Zonally Averaged Mass Transport Circulation in the Troposphere. J. Atmos. Sci., 56, 1688-1697.

Houze, R. A., Jr., S. S. Chen, D. E. Kingsmill, Y. Serra, and S. E. Yuter, 2000: Convection over the Pacific warm pool in relation to the atmospheric Kelvin-Rossby wave. J. Atmos. Sci., 57, 3058-3089.

Khairoutdinov, M. F., and D. A. Randall, 2003: Cloud-resolving modeling of the ARM summer 1997 IOP: Model formulation, results, uncertainties, and sensitivities. J. Atmos. Sci., 60, 607-625.

Khouider, B. and Y. Han, 2013: Simulation of convectively coupled waves using WRF: a framework for assessing the effects of mesoscales on synoptic scales. Theoretical and Computational Fluid Dynamics. Volume 27, Issue 3-4, 473-489.

Kjellsson, J., K. Doos, Kristofer, F. Lalibert, and J. Zika, 2014: The Atmospheric General Circulation in Thermodynamical Coordinates. Journal of the Atmospheric Sciences, 71, 916-928.

Laliberté F., J. Zika. L. Mudryk, P. Kushner, J. Kjellsson, K. Doos, 2015: Constrained work output of the moist atmospheric heat engine in a warming climate. Science, 347, 540-543.

Madden, R., and P. Julian, 1972: Description of global- scale circulation cells in the tropics with a 40-50-day period. J. Atmos. Sci., 29, 1109-1123.

Mahoney, K. M. and G. M. Lackmann, 2011: The Sensitivity of Momentum Transport and Severe Surface Winds to Environmental Moisture in Idealized Simulations of a Mesoscale Convective System. Mon. Wea. Rev., 139, 1352-1369.

Malinowski, Sz., A. Wyszogrodzki, and M. Ziemianski, 2011: Modeling atmospheric circulations with sound-proof equations. Acta Geophysica, 59(6), 1073-1075.

Mapes, B. E., 1993: Gregarious Tropical Convection. J. Atmos. Sci., 50, 2026-2037. doi: http://dx.doi.org/10.1175/1520-0469(1993)050¡2026:GTC¿2.0.CO;2

McIntosh, P. C., and T. J. McDougall, 1996: Isopycnal averaging and the residualmean circulation. J. Phys.Oceanogr., 26, 1655-1660.

Moncrieff, M. W., 1981: A theory of organized steady convection and its transport properties. Quart. J. Roy. Meteor. Soc., 107, 29-50.

Moncrieff, M. W., 1992: Organized convective systems: Archetypal models, mass and momentum flux theory, and parameterization, Quart. J. Roy. Meteor. Soc., 118, 819-850.

Moncrieff, M. W., D. E. Waliser, M. J. Miller, M. A. Shapiro, G. R. Asrar and J. Caughey, 2012: Multiscale Convective Organization and the YOTC Virtual Global Field Campaign. Bull. Amer. Meteor. Soc., 93, 1171-1187. doi: http://dx.doi.org/10.1175/BAMS-D-11-00233.1

Pauluis, O., A. Czaja, and R. Korty, 2008: The global atmospheric circulation on moist isentropes. Science, 321, 1075-1078. doi:10.1126/science.1159649.

Pauluis, O., A. Czaja, and R. Korty, 2010: The global atmospheric circulation in moist isentropic coordinates. J. Climate, 23, 3077-3093.

Pauluis, O. M. and A. A. Mrowiec, 2013: Isentropic Analysis of Convective Motions. J. Atmos. Sci., 70, 3673-3688.

Prusa, J.M., P. Smolarkiewicz, and A. Wyszogrodzki, 2008: EULAG, a computational model for multiscale flows. Computers & Fluids, 37, 1193-1207.

Rio, C., F. Hourdin, J.-Y. Grandpeix, and J.-P. Lafore, 2009: Shifting the diurnal cycle of parameterized deep convection over land. Geophys. Res. Lett., 36, L07809. doi:10.1029/2008GL036779.

Roundy, P. and W. Frank, 2004: A climatology of waves in the equatorial region. J. Atmos. Sci., 61(17), 2105-2132.

Sanderson B.M., Shell K.M. and W. Ingram, 2010: Climate feedbacks determined using radiative kernels in a multi-thousand member ensemble of AOGCMs. Clim. Dyn., 30, 175-190.

Schumacher, C., and R. A. Houze Jr., 2003: Stratiform rain in the tropics as seen by the TRMM Precipitation Radar. J. Climate, 16, 1739-1756.

Slawinska J., O. Pauluis, Andrew J. Majda, and W. W. Grabowski, 2014: Multiscale Interactions in an Idealized Walker Circulation: Mean Circulation and Intraseasonal Variability. J. Atmos. Sci., 71, 953-971.

Smolarkiewicz, P, 2006: Multidimensional positive definite advection transport algorithm: an overview. Int. J. Numer. Methods. Fluids. 50,1123-1144.

Stechmann, S., A. J. Majda, and D. Skjorshammer, 2013: Convectively coupled wave-environment interactions. Theor. Comput. Fluid Dyn. 27: 513-532 DOI 10.1007/s00162-012-0268-8.

Townsend, R. D., and D. R. Johnson, 1985: A diagnostic study of the isentropic zonally averaged mass circulation during the first GARP global experiment. J. Atmos. Sci., 42, 1565-1579.

Trenberth, Kevin E., Aiguo Dai, Roy M. Rasmussen, David B. Parsons, 2003: The Changing Character of Precipitation. Bull. Amer. Meteor. Soc., 84, 1205-1217.

Tung, W.-W., and M. Yanai, 2002a: Convective momentum transport observed during the TOGA COARE IOP. Part I: General features. J. Atmos. Sci., 59, 1857-1871.

Tung, W.-W., and M. Yanai, 2002b: Convective momentum transport observed during the TOGA COARE IOP. Part II: Case studies. J. Atmos. Sci., 59, 2535-2549.

Wheeler, M. and G.N. Kiladis, 1999: Convectively coupled equatorial waves: analysis of clouds and temperature in the wavenumber-frequency domain. J. Atmos. Sci. 56(3), 374-399.

Wu, X. and M. Yanai, 1994: Effects of Vertical Wind Shear on the Cumulus Transport of Momentum: Observations and Parameterization. J. Atmos. Sci., 51, 1640-1660.

Wu, X., W. W. Grabowski, and M. W. Moncrieff, 1998: Long-term behavior of cloud systems in TOGA COARE and their interactions with radiative and surface processes. Part I: Two-dimensional Modeling Study. J. Atmos. Sci., 55, 2693-2714.

Yang, G., Hoskins, B., Slingo, J., 2007: Convectively coupled equatorial waves. Part I: horizontal and vertical structures. J. Atmos.Sci., 64(10), 3406-3423.

Zika, J., M. England, and W.P. Sijp, 2012: The Ocean Circulation in Thermohaline Coordinates. Journal of Physical Oceanography, 42, 708-724.

## LIST OF FIGURES

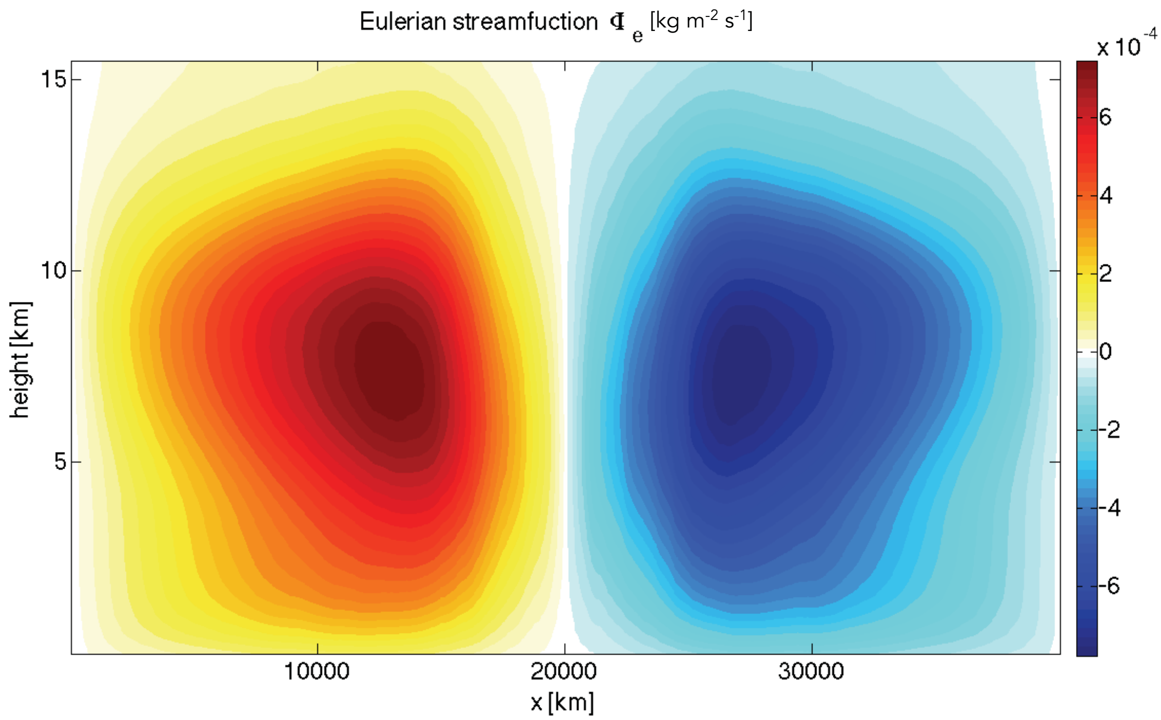


FIG. 1. Eulerian streamfunction [kg $m^{-2}$ $s^{-1}$]. X axis: horizontal dimension (km). Y axis: height (km).

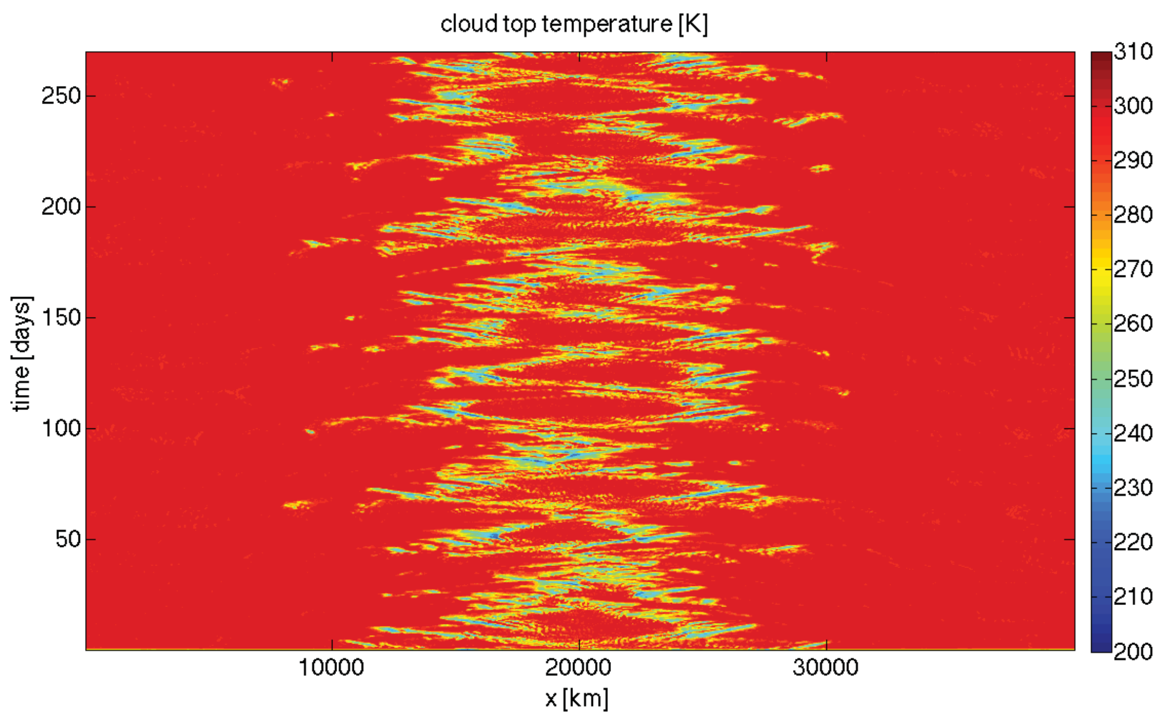


FIG. 2. Hovmoller diagram of the cloud top temperature (K). X axis: horizontal dimension (km). Y axis: time (days).

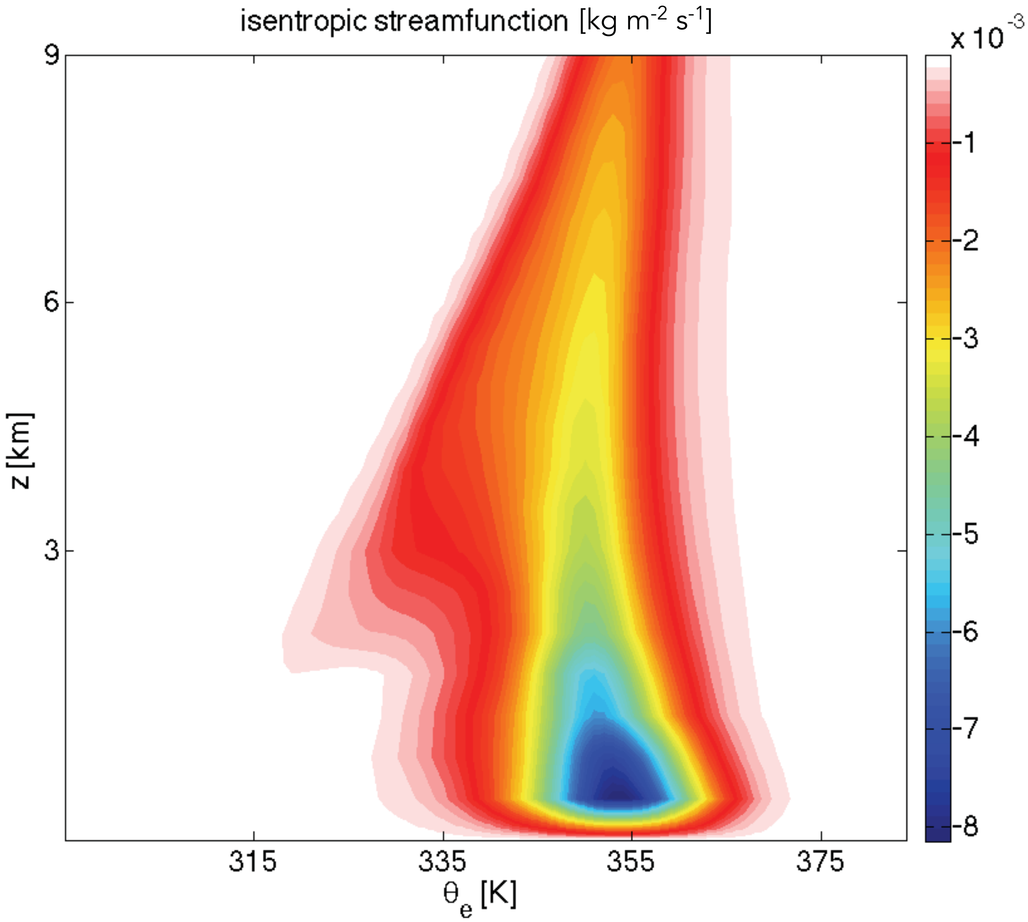


646 FIG. 3. Mean isentropic streamfunction [kg m$^{-2}$ s$^{-1}$] averaged over 273 days and 40,000 km. X axis:
647 equivalent potential temperature (K). Y axis: height (km).

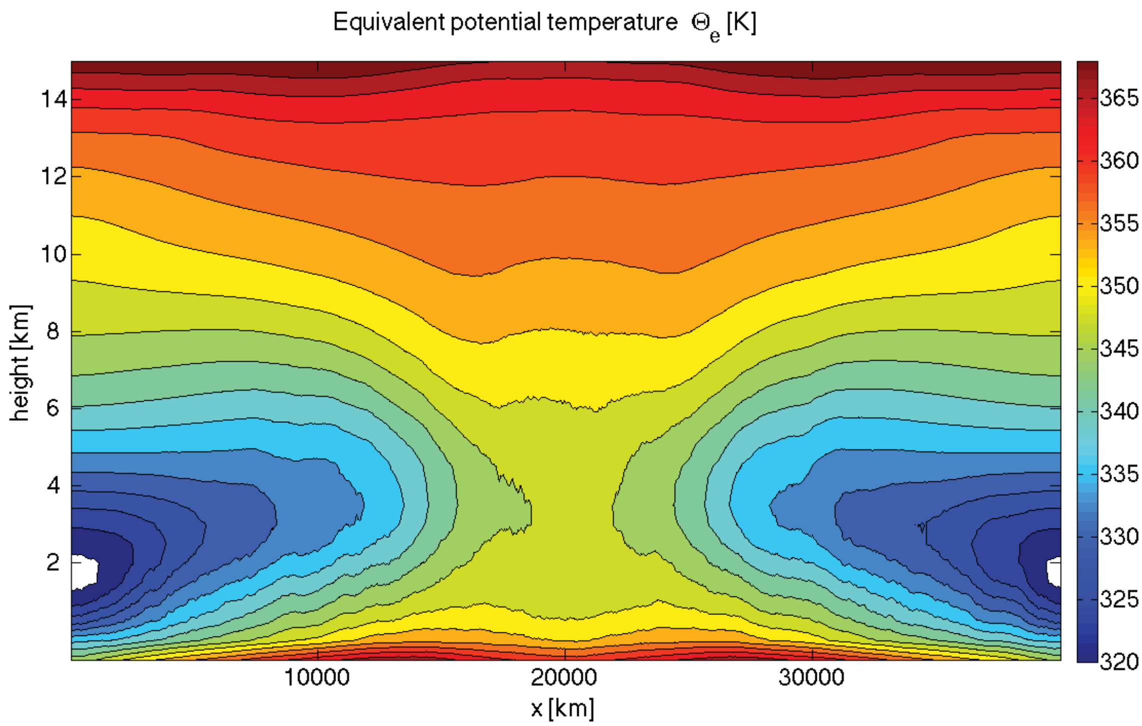


FIG. 4. Mean distribution of the equivalent potential temperature (K). X axis: horizontal dimension (km). Y axis: height (km).

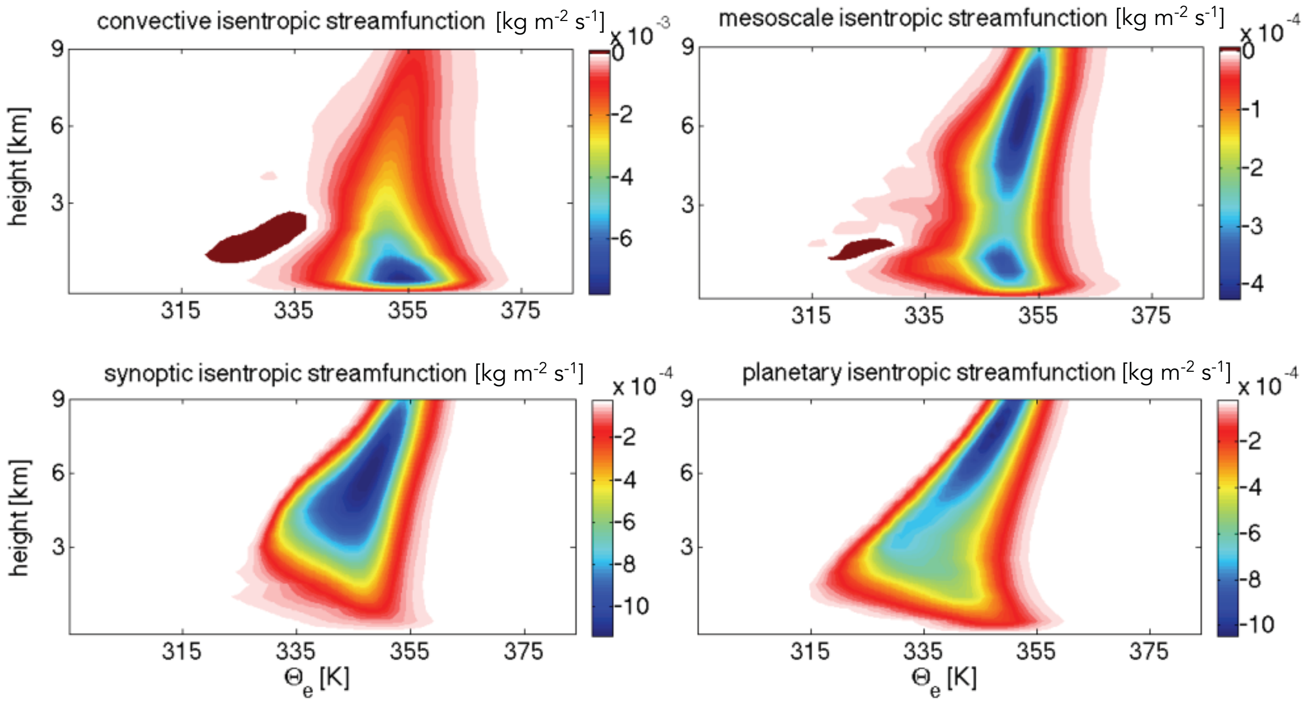


FIG. 5. Isentropic streamfunction [kg m$^{-2}$ s$^{-1}$] associated with the convective (upper left), mesoscale (upper right), synoptic (lower left), and planetary (lower right) scales averaged over 273 days and 40,000 km. X axis: equivalent potential temperature (K). Y axis: height (km).

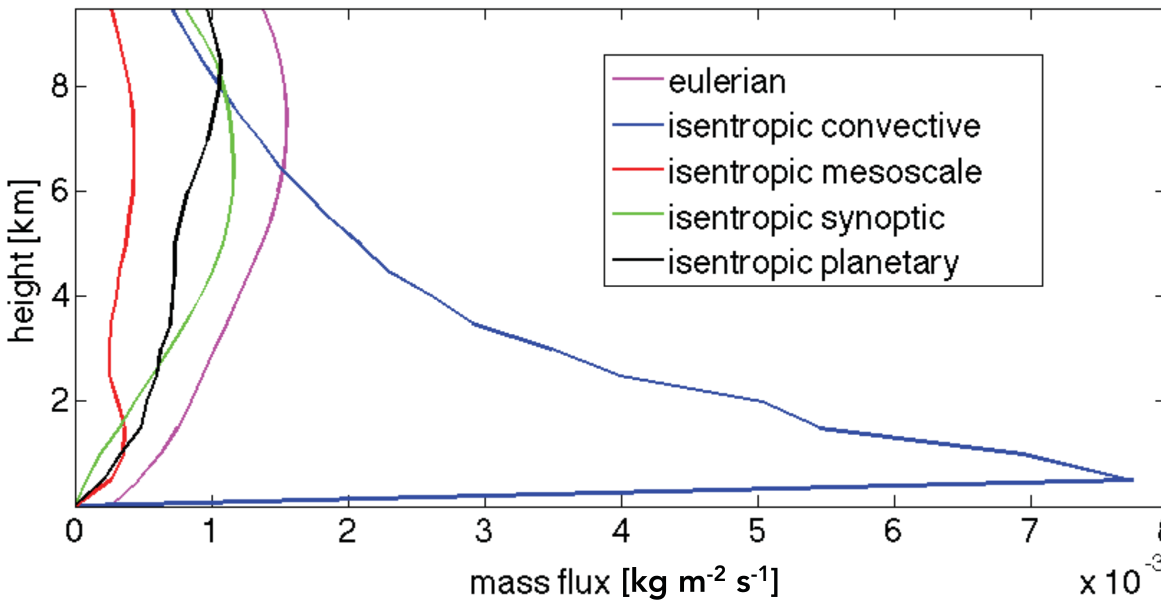


FIG. 6. Vertical mass fluxes [kg $m^{-2}$ $s^{-1}$] associated with the convective (blue line), mesoscale (red line), synoptic (green line), and planetary (black line) scales averaged over 273 days and 40,000 km. Y axis: height (km).

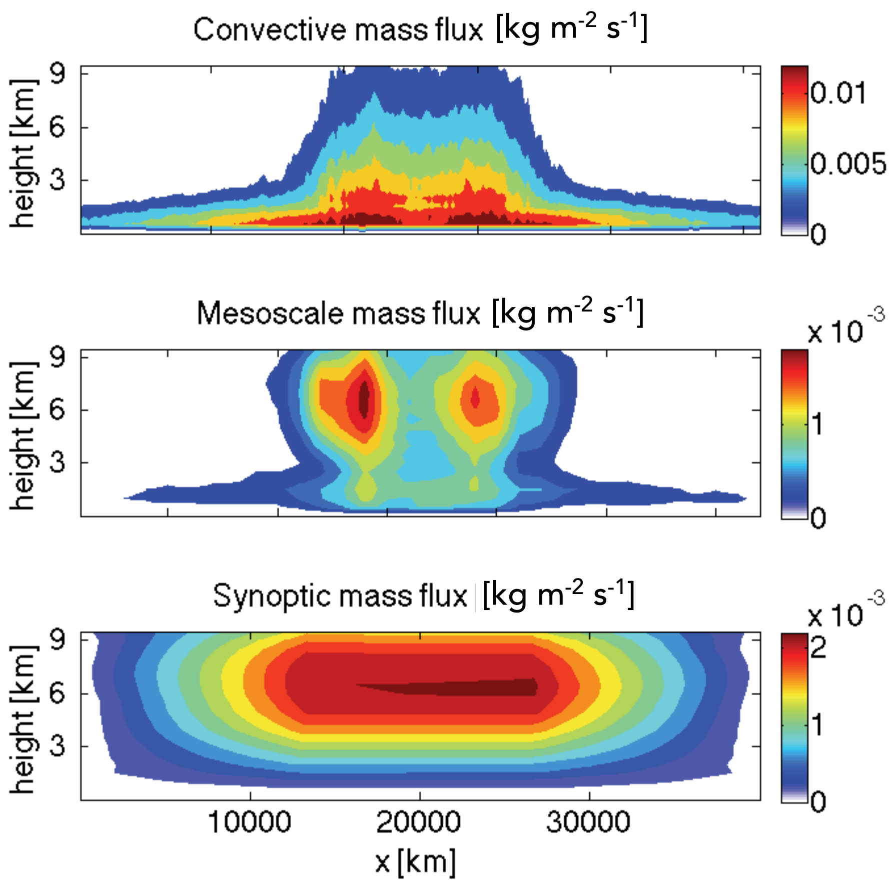


FIG. 7. Time-averaged spatial distribution of the convective (top), mesoscale (middle), and synoptic scale (bottom) mass fluxes. X axis: horizontal dimension (km). Y axis: height (km).

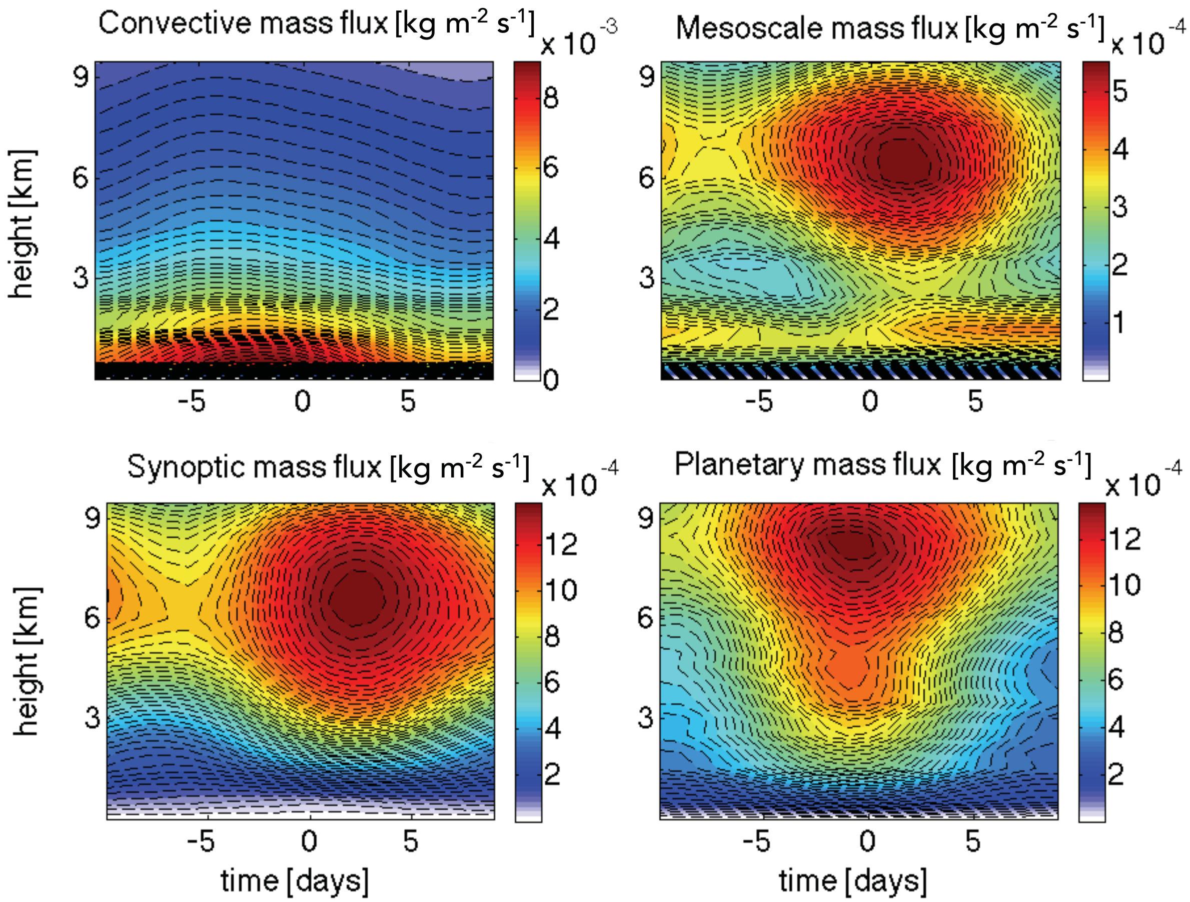


FIG. 8. Lag regression of the domain-averaged vertical mass fluxes associated with the convective (upper left), mesoscale (upper right), synoptic (lower left), and planetary (lower right) scales. X axis: time (days). Y axis: height (km).

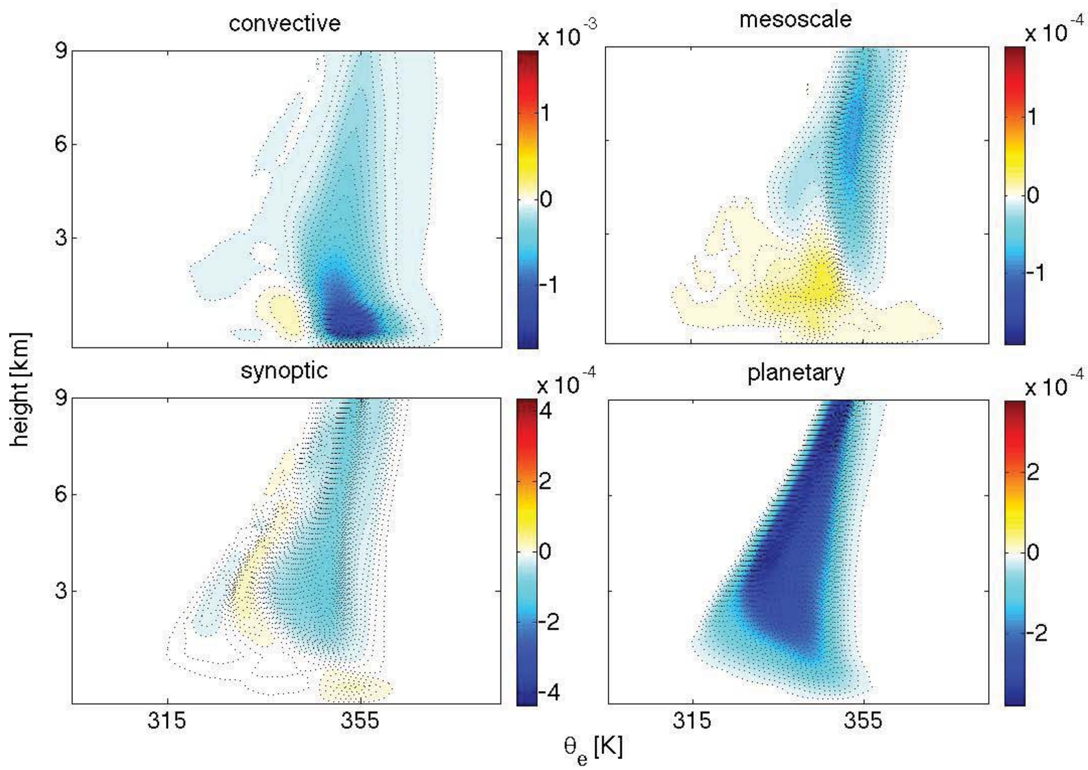


FIG. 9. Means (first and third columns) and anomalies (second and fourth columns) in the isentropic streamfunctions associated with the convective (upper left), mesoscale (upper right), synoptic (lower left), and planetary (lower right) scale averaged over the whole domain and day -1 of the low-frequency cycle.

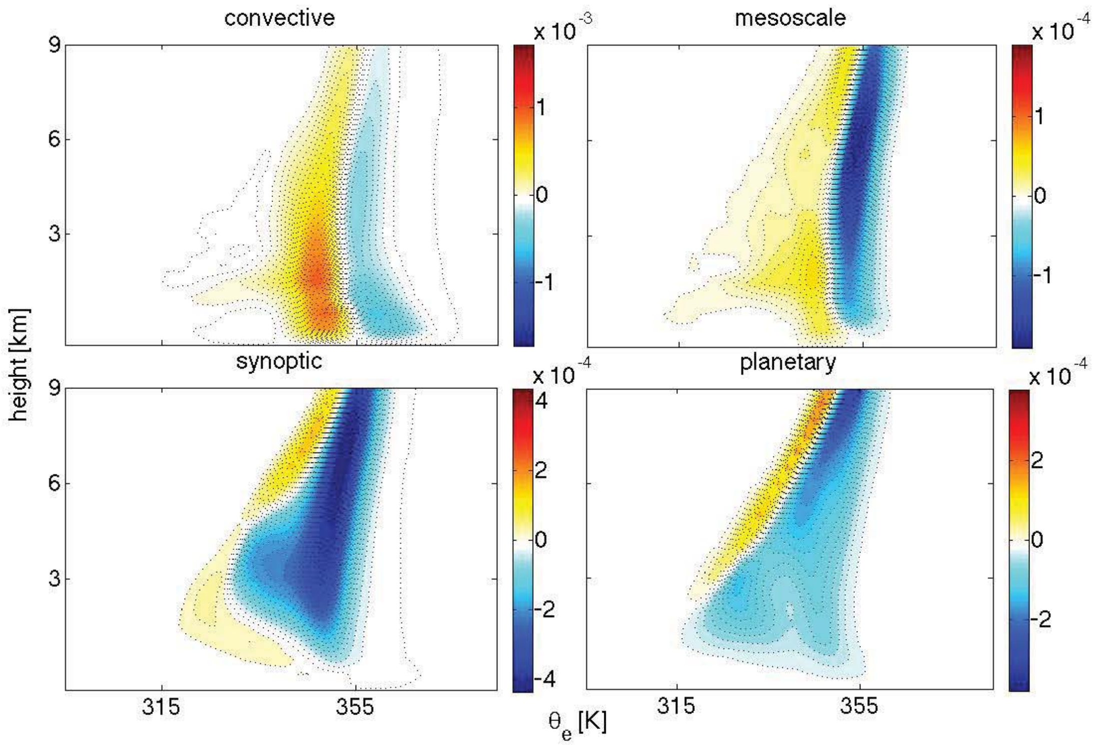


FIG. 10. Means (first and third columns) and anomalies (second and fourth columns) in the isentropic streamfunctions associated with the convective (upper left), mesoscale (upper right), synoptic (lower left), and planetary (lower right) scales averaged over the whole domain and day 4 of the low-frequency cycle.

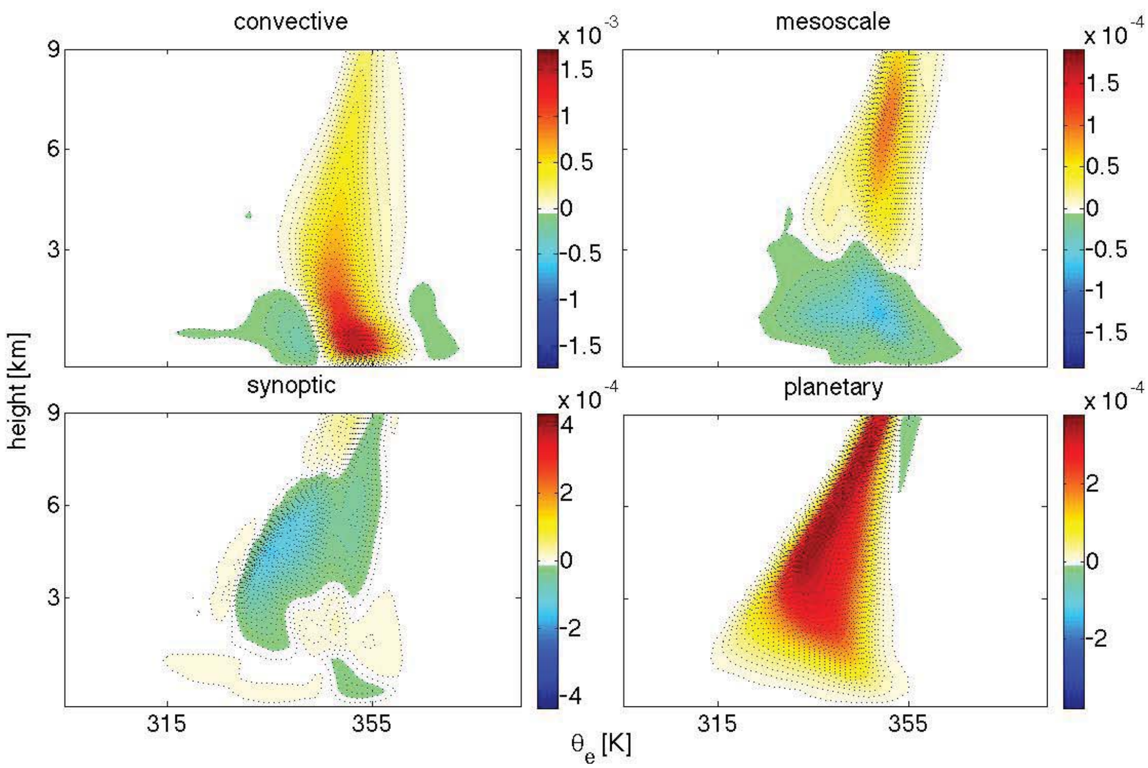


FIG. 11. Means (first and third columns) and anomalies (second and fourth columns) in the isentropic streamfunctions associated with the convective (upper left), mesoscale (upper right), synoptic (lower left), and planetary (lower right) scales averaged over the whole domain and day 9 of the low-frequency cycle.

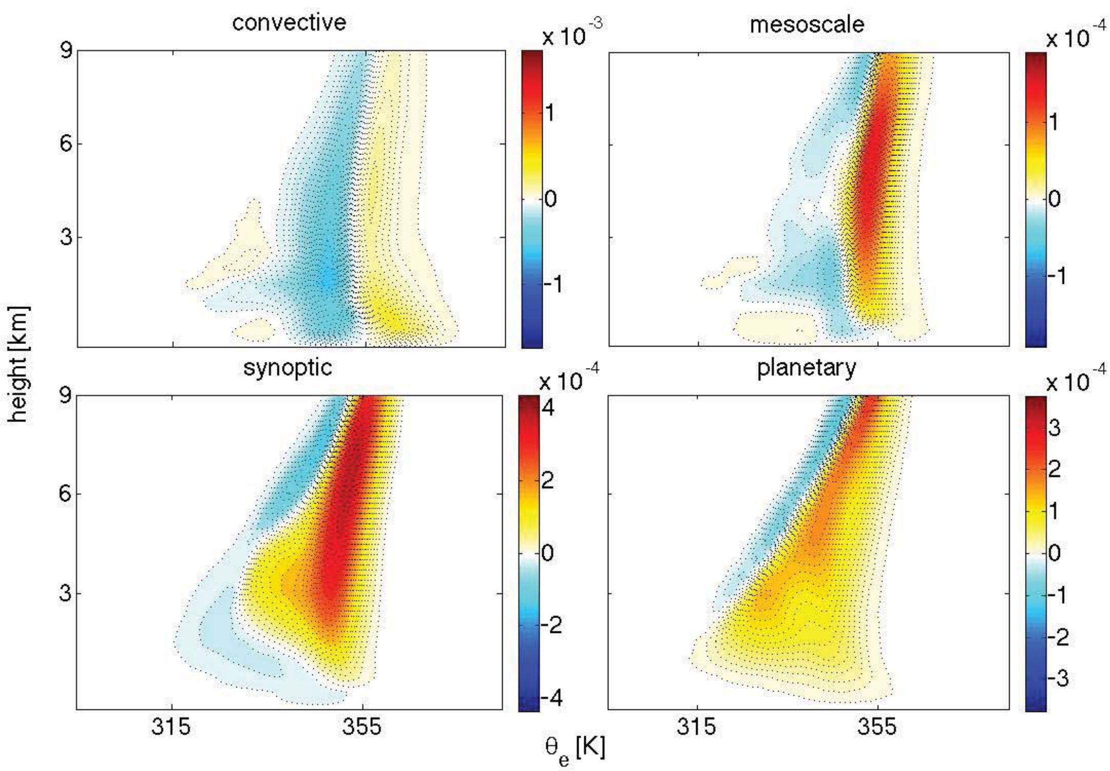


FIG. 12. Means (first and third columns) and anomalies (second and fourth columns) in the isentropic streamfunctions associated with the convective (upper left), mesoscale (upper right), synoptic (lower left), and planetary (lower right) scales averaged over the whole domain and day -6 of the low-frequency cycle